



MOF-derived hierarchical core-shell hollow iron-cobalt sulfides nanoarrays on Ni foam with enhanced electrochemical properties for high energy density asymmetric supercapacitors

Kai Le^a, Mengjiao Gao^b, Wei Liu^{a,*}, Jiurong Liu^{b, **}, Zhou Wang^b, Fenglong Wang^b, Vignesh Murugadoss^{c,d,e}, Shide Wu^f, Tao Ding^{g, ***}, Zhanhu Guo^{c, ****}

^a Institute of Crystal Materials, Shandong University, Shandong, 250100, China

^b School of Materials Science and Engineering, Shandong University, Jinan, Shandong, 250061, China

^c Integrated Composites Laboratory (ICL), Department of Chemical & Biomolecular Engineering, University of Tennessee, Knoxville, USA

^d College of Chemical and Environmental Engineering, Shandong University of Science and Technology, Qingdao, Shandong, 266590, China

^e Key Laboratory of Materials Processing and Mold (Zhengzhou University), Ministry of Education, National Engineering Research Center for Advanced Polymer Processing Technology, Zhengzhou University, Zhengzhou, China

^f Henan Provincial Key Laboratory of Surface and Interface Science, Zhengzhou University of Light Industry, No. 136, Science Avenue, Zhengzhou, 450001, China

^g College of Chemistry and Chemical Engineering, Henan University, Kaifeng, 475004, China



ARTICLE INFO

Article history:

Received 7 June 2019

Received in revised form

7 August 2019

Accepted 4 September 2019

Available online 7 September 2019

Keywords:

Metal-organic frameworks

Core-shell

Hollow

Iron-cobalt sulfides

Supercapacitors

ABSTRACT

In this work, hierarchical core-shell hollow iron-cobalt sulfides nanoarrays supported on conductive nickel foam (Fe-Co-S/NF) were fabricated using metal-organic frameworks (MOFs) as the sacrificial templates. Delicately manipulating the etching/ion-exchange reaction between Co-MOF and FeSO_4 and the subsequent solvothermal sulfurization led to the formation of hierarchical core-shell hollow nanostructure with FeCo_2S_4 -nanosheets shell assembled on the Co_3S_4 hollow nanoarrays. Owing to the complex composition and unique structure, the obtained Fe-Co-S/NF possessed abundant electroactive sites, short charge/ion diffusion path, rich redox reactions and good structural robustness, contributing to the boosted electrochemical performance as supercapacitor electrodes. Consequently, the obtained Fe-Co-S/NF electrode exhibited a specific capacitance of 2695 F g^{-1} at 1 A g^{-1} , a favorable rate capability with 69.8% capacitance retention at 10 A g^{-1} (much higher than that of CoS/NF electrode, i.e., 36.3%), and a retention of 84% over 1000 cycles. Moreover, an asymmetric supercapacitor was assembled by engaging Fe-Co-S/NF and reduced graphene oxide (rGO) as cathode and anode, respectively. The obtained device delivered a high energy density of 43.6 W h kg^{-1} at a power density of 770 W kg^{-1} , while maintaining a capacity retention of 89.6% after 5000 cycles. The robust electrochemical properties indicate that the Fe-Co-S/NF can be used as promising electrode materials for high performance supercapacitors applications.

© 2019 Elsevier Ltd. All rights reserved.

1. Introduction

Supercapacitors, with excellent power density, fast charge-discharge, and outstanding long-term cycling stability, have recently attracted great research interests, due to the rapidly increasing demand for high-performing energy storage and

conversion devices [1–6]. Currently, although various carbon-based materials are the most studied electrode materials for electron double-layer capacitors (EDLCs) [7,8], their large-scale applications are still hindered by their low energy density [9,10]. Compared with carbon materials, pseudocapacitive materials, such as conducting polymers and transition metal oxides/hydroxides/sulfides, possess much higher electrochemical capacitance because of the abundant faradaic redox reactions [11]. In particular, transition metal sulfides, with the merits of higher intrinsic conductivity and electrochemical activity than their metal oxides/hydroxides counterparts, have recently gained extensive attention and have been regarded as considerable candidates for supercapacitors [12]. In previous reports, researches have shown the potential of cobalt

* Corresponding author.

** Corresponding author.

*** Corresponding author.

**** Corresponding author.

E-mail addresses: weiliu@sdu.edu.cn (W. Liu), jrliu@sdu.edu.cn (J. Liu), dingtao@henu.edu.cn (T. Ding), zguo10@utk.edu (Z. Guo).

sulfide [13], nickel sulfide [14], and their compounds [15] for supercapacitors. In particular, ternary metal sulfides, such as NiCo_2S_4 [16] and ZnCo_2S_4 [17], with a richer electrochemical activity and a higher electrical conductivity, have been regarded as promising electrode materials for supercapacitors, because the multiple oxidation states of ternary metal sulfides can provide much richer redox reactions than single metal sulfides [18]. Recently, FeCo_2S_4 is reported to achieve a specific capacitance of 2411 F g^{-1} , which is higher than most ternary sulfides, due to the variable valences of Fe^{3+} during the redox reactions [19].

Fabricating advantageous nanostructures for electrode materials has been considered as an effective strategy for improving electrochemical performance. Especially, the core-shell hollow nanostructures can significantly improve the performance of electrodes due to numerous accessible active sites and the synergistic effects between core and shell substances [20,21]. However, it is still a challenge to fabricate complex core-shell hollow nanostructures owing to the difficulties for delicately manipulating the chemical reactions and the structural compatibility between different subunits [22].

Metal-organic frameworks (MOFs), have been widely studied to construct functional materials with sophisticated structure [23–25]. In previous reports, MOF-derived transition metal sulfides with special nanostructure, such as cobalt sulfide nanoarrays [26], nickel sulfide nanorods [27], nickel-cobalt sulfide nanocages [28], and zinc-cobalt sulfide nanosheet arrays [29], have been employed as electrodes for high-performance supercapacitors. Furthermore, the direct growth of MOFs array on a conductive substrate (nickel foam, carbon cloth, etc.) is beneficial for the electrochemical behavior. The agglomeration can be avoided when MOF-derived transition metal sulfides are used owing to the oriented growth of MOF nanoarrays on the conductive substrate. These ordered nanostructures can significantly improve the utilization of electroactive materials [30]. In addition, strong adhesion between electroactive materials and conductive substrates avoids the use of nonconductive binder and ensures a remarkable cycling stability of the electrodes. However, to the best of our knowledge, the synthesis of iron-cobalt sulfides derived from MOFs as electrode materials for supercapacitors has not been reported yet.

Herein, complex hierarchical core-shell hollow nanostructures grown on nickel foam were synthesized with FeCo_2S_4 -nanosheets assembled on the surface of Co_3S_4 hollow nanoarrays. These 2D Co-MOF nanoarrays were firstly assembled on nickel foam (Co-MOF/NF) via a simple solution reaction. Then, the ion-exchange/etching process within FeSO_4 aqueous solution led to form iron-cobalt layered double hydroxides (FeCo-LDHs) on the surface of Co-MOF nanoarrays. After the subsequent solvothermal sulfurization, iron-cobalt sulfides nanoarrays with a hierarchical core-shell hollow nanostructure on Ni foam were obtained. The hollow core Co_3S_4 nanoarrays directly grown on nickel foam served as the electron transmission channel and provided more accessible active sites. The shell of FeCo_2S_4 -nanosheets provided larger electrode/electrolyte contacting areas and additional pseudo-capacitance. As expected, the Fe-Co-S/NF exhibited an excellent specific capacitance of 2695 F g^{-1} at 1 A g^{-1} , much higher than that of Co_3S_4 sample (1500 F g^{-1}). Furthermore, an asymmetric supercapacitor (ASC) device assembled by Fe-Co-S/NF (cathode) and rGO (anode) achieved a high energy density (43.6 Wh kg^{-1}) and outstanding long-term cycling stability (about 89.6% capacitance retention after 5000 cycles).

2. Experimental

2.1. In-situ growth of the Co-MOF on nickel foam

In a typical process, 40 mL aqueous $\text{Co}(\text{NO}_3)_2 \cdot 6\text{H}_2\text{O}$ solution

(50 mM) was quickly added into a 40 mL aqueous solution of 2-Methylimidazole (Hmim, 0.4 M). After stirring for 5 min, a piece of nickel foam ($1 \times 2 \text{ cm}^2$) was immersed into the above solution for 3 h at room temperature. After that, the sample was taken out, washed and then dried at 60°C overnight.

2.2. Synthesis of LDH@co-MOF/NF

A piece of Co-MOF/NF was immersed into 100 mL aqueous $\text{FeSO}_4 \cdot 7\text{H}_2\text{O}$ solution (10 mM). After reacting for 5 min, the sample was taken out, washed and dried at 60°C overnight.

2.3. Synthesis of Fe-Co-S/NF

A piece of as-obtained LDH@Co-MOF was placed into a Teflon-lined autoclave containing 1.6 mmol thioacetamide (TAA) and 40 mL ethanol. After heating at 120°C for 4 h, the Fe-Co-S/NF was fetched out, washed and dried at 60°C overnight. The mass loading of iron-cobalt sulfides on nickel foam was estimated to be $\sim 2.4 \text{ mg cm}^{-2}$.

For comparison, cobalt sulfides supported on nickel foam (CoS/NF) were prepared through vulcanizing Co-MOF/NF with the same conditions, and the mass loading of CoS/NF was about 2.0 mg cm^{-2} .

2.4. Synthesis of rGO negative electrode

Graphene oxide (GO) was obtained using modified Hummer's method [31]. Briefly, 80 mg GO powders were dispersed in 40 mL methanol with intensive sonication. Then, 1 mL aqueous ammonia (25% $\text{NH}_3 \cdot \text{H}_2\text{O}$) was added into the above solution at room temperature with stirring for 0.5 h. Then, the as-obtained suspension was sealed into a Teflon-lined autoclave. After heating at 180°C for 12 h, the black precipitate was harvested, washed and dried in vacuum. Next, the mixed slurry of rGO power (80%), acetylene black (10%), and PVDF (10%) was prepared using N-Methyl-2-pyrrolidone (NMP) as solvent. A clean nickel foam ($2 \times 2 \text{ cm}^2$) was coated with the slurry and dried in vacuum at 100°C overnight, followed by pressing at 10 MPa for 10 s. As a result, the mass loading of rGO coated on nickel foam was about 2.1 mg cm^{-2} .

2.5. Characterizations

X-ray powder diffractions (XRD) were conducted using the Rigaku DMax-RC X-ray diffractometer to analyze the crystallization of the as-prepared samples. Scanning electron microscope (SEM) images and energy dispersive X-ray spectroscopy (EDX) mapping images were obtained using the field-emission scanning electron microscope (FE-SEM, JEOL, JSM-6700F, 10 kV). The morphology and microstructure of the samples were investigated by using the high-resolution transmission electron microscope (HR-TEM, JEOL, JEM-2100, 200 kV). The X-ray photoelectron spectrum (XPS) of as-prepared sample was recorded using Kratos Analytical spectrometer to determine the surface properties.

2.6. Electrochemical measurements

The electrochemical performances of as-made working electrodes were first characterized by cyclic voltammogram (CV), galvanostatic charge-discharge (GCD) and electrochemical impedance spectra (EIS) on an Iviumstat electrochemistry work station in a three-electrode system including the as-made working electrode, a Pt foil counter electrode, a saturated calomel electrode (SCE) reference electrode, and a 1 M KOH aqueous electrolyte. The specific capacitances can be determined from GCD curves through formula (1) [32]:

$$C = \frac{I \times \Delta t}{m \times \Delta V} \quad (1)$$

where Δt , I , and ΔV are the discharge time, the charge-discharge current, and the potential range excluding IR drop in the charge-discharge curves, and m represents the mass loading of the working electrode.

2.7. The fabrication process of asymmetric supercapacitor (ASC)

The ASC devices were fabricated using rGO as anode and Fe-Co-S/NF as cathode, respectively. Typically, two as-prepared electrodes with a separator were stacked and further immersed into 1 M KOH solution. Taking into account the charge storage performances of cathode and anode, the mass ratio of two electrodes was determined by Equation (2) [9]:

$$\frac{m_+}{m_-} = \frac{C_- \Delta V_-}{C_+ \Delta V_+} \quad (2)$$

where m , V , and C represent the mass loading, potential range and specific capacitance of cathode (+) and anode (-), respectively. The specific capacitance, energy density, and power density of ASC device were calculated by formulas (3–5) [33]:

$$C_{cell} = \frac{I \times \Delta t}{m \times \Delta V} \quad (3)$$

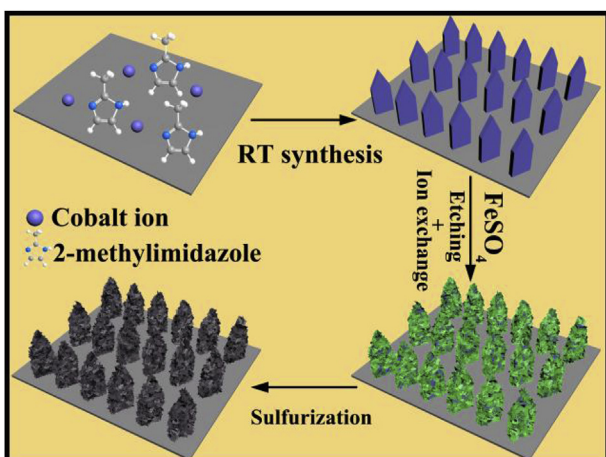
$$E = \frac{1}{2} C_{cell} \Delta V^2 \quad (4)$$

$$P = \frac{E}{\Delta t} \quad (5)$$

where C_{cell} , ΔV , and Δt are the corresponding parameters in discharge curves, and m represents the total mass loading of two electrode in ASC device.

3. Results and discussion

Scheme 1 displays the fabrication process for the nanoarrays of iron-cobalt sulfides on the nickel foam (see the Experimental Section for details). First, 2D Co-MOF nanoarrays directly grew on nickel foam at room temperature using cobalt ion and Hmim as



Scheme 1. Schematic illustration of the fabrication of Fe-Co-S/NF.

metal ion and organic linker in aqueous solution. As shown in Fig. S1a (supporting information), the color of the Co-MOF/NF was navy blue. Subsequently, through an ion exchange/etching process in FeSO_4 aqueous solution for 5 min, the Co-MOF nanoarrays were etched and simultaneously the FeCo-LDH was deposited on the surface, resulting in a core-shell structure. In this step, Co-MOF was gradually etched by the protons released from the hydrolysis of Fe^{2+} , and the co-precipitation of Co^{2+} and Fe^{2+} caused the generation of FeCo-LDH on the surface of nanoarrays [34]. Obviously, the color of the sample changed from navy blue to purple after the ion exchange/etching process (Fig. S1b). After a solvothermal treatment in TAA solution at 120 °C for 4 h, the LDH@Co-MOF was sulfurized to yield iron-cobalt sulfides with hollow core-shell structure, and the sample accordingly changed from purple to dark (Fig. S1c). The as-prepared Fe-Co-S/NF was used as an electrode of supercapacitors in the following studies.

The structure evolution from Co-MOF nanoarrays to the nanoarrays of iron-cobalt sulfides was revealed by SEM characterization. Fig. 1a indicates the uniform coverage of the Co-MOF nanoarrays on nickel foam. From the enlarged image (Fig. 1b), the Co-MOF nanoarrays display an average thickness of ~300 nm. The XRD pattern of Co-MOF/NF in Fig. S2 is well consistent with the XRD patterns of the Co-MOF reported previously [35]. As shown in Fig. 1c, nanoflakes appear on the surface of nanoarrays after the ion exchange/etching process. In addition to the characteristic diffraction peaks of nickel and Co-MOF, the XRD pattern of LDH@Co-MOF/NF (the red plot in Fig. S2) shows the peaks at 11.0°, 22.2°, and 60.3°, which are assigned to the (003), (006), and (113) planes of the hydrotalcite-like LDH [36–38]. The results demonstrate that LDH have been successfully generated on the surface of Co-MOF during the ion exchange/etching process. After sulfurization, the nanoarrays structure with intersecting nanosheets coating was completely maintained, as shown in Fig. 1d. As shown in EDX mapping images (Fig. S3), all elements are well dispersed, which agrees well with the SEM image and suggests that the Fe-Co-S nanoarrays are uniformly assembled onto the Ni foam. Besides, as shown in the SEM image of CoS/NF (Fig. S4), the solid Co-MOF nanoarrays have been transformed to hollow CoS nanoarrays after sulfurization. Furthermore, the morphological evolution of Co-MOF at different reaction time with FeSO_4 aqueous solution was investigated by SEM. As shown in Fig. S5, decreasing the soaking time to 2 min results in poor LDH nanosheets deposited on the surface of Co-MOF, while prolonging the soaking time to 10 min results in the overgrowth of nanosheets. When reacting for 10 min, the Co-MOF nanoarrays have been completely destroyed. To get hierarchical core-shell nanostructures, 5 min was considered as the optimal time for the reaction between Co-MOF and FeSO_4 aqueous solution.

The detailed morphology and nanostructure of the as-prepared nanoarrays of the iron-cobalt sulfides were further revealed by TEM. Fig. 2a and b depicts that in the core-shell hollow structured iron-cobalt sulfides, the FeCo_2S_4 nanosheets wrap up the hollow Co_3S_4 . The selected area electron diffraction (SAED) pattern (Fig. 2c) displays a set of concentric rings, indicating the polycrystalline nature of iron-cobalt sulfides nanoarrays, and the reflections from the (311) and (440) planes correspond to the Co_3S_4 phase (JCPDS card no. 42–1448). In the HR-TEM image (Fig. 2d), the measured lattice fringe of 0.299 nm is ascribed to the (440) plane of Co_3S_4 (JCPDS card no. 42–1448), and the distance of 0.287 nm is according to the (311) plane of FeCo_2S_4 phase [39,40].

The constituents and crystalline phase of as-made samples were investigated using XRD. Both the patterns in Fig. 3 show three characteristic diffraction peaks of nickel. The XRD pattern of CoS/NF shows the diffraction peaks at 31.4°, 38.1°, 55.0°, 64.8°, and 77.7°, which represent the (311), (400), (400), (533), and (731) planes of Co_3S_4 (JCPDS card no. 42–1448). Apart from the peaks at 64.8° and

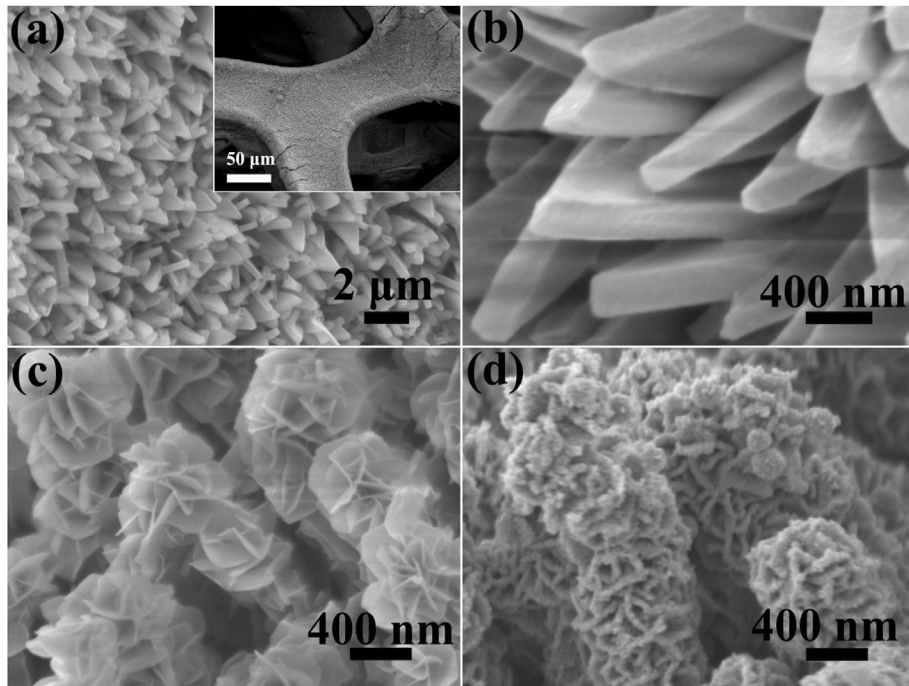


Fig. 1. SEM images of (a and b) Co-MOF/NF, (c) LDH@Co-MOF/NF, and (d) Fe-Co-S/NF.

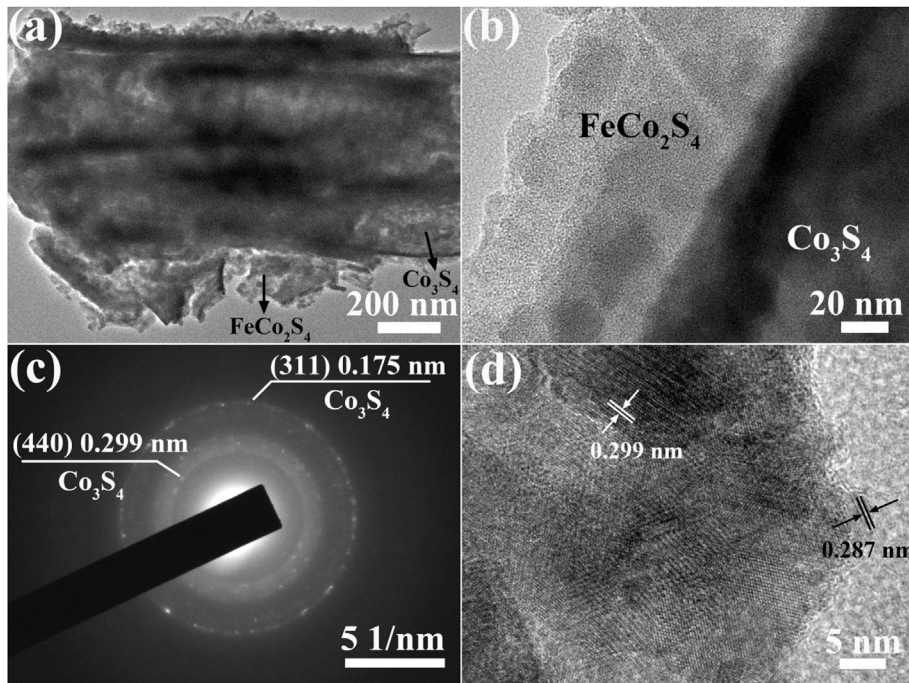


Fig. 2. (a, and b) TEM image, (c) the selected-area electron diffraction pattern, and (d) HR-TEM image of iron-cobalt sulfides scraped off from the nickel foam.

77.7°, the Fe-Co-S/NF shows the diffraction peaks at 21.8°, 31.1°, and 49.1°, which are consistent with the patterns of FeCo₂S₄ in the previous reports [40]. The results further confirm that the composites are composed of FeCo₂S₄ and Co₃S₄. Besides, the diffraction peaks at 20° and 22° in both patterns could be ascribed to the S (JCPDS card no. 24–1251) produced by TAA decomposition [41].

The XPS measurement is used to study the surface elemental composition and chemical properties in Fe-Co-S/NF. In Fig. 4a, the

Co, Fe, O, C and S elements can be identified in the XPS survey spectrum, and the presence of C 1s and O 1s peaks may be owing to the exposure to the air. As presented in Fig. 4b, the S 2p spectrum is deconvoluted to two peaks at 163.5 and 162.1 eV, which are consistent with the S 2p_{1/2} and S 2p_{3/2} signals of S²⁻, while the peak at 168.8 eV is a satellite peak [42]. In the spectrum of Co 2p (Fig. 4c), the Co 2p_{1/2} peak and Co 2p_{3/2} peak can be observed at 793.9 and 778.9 eV with a distance of ~15 eV, which can be indexed to the

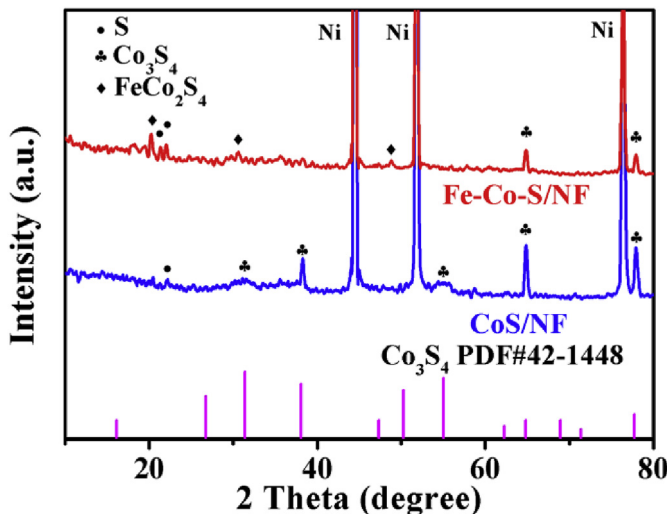


Fig. 3. XRD patterns of CoS/NF and Fe-Co-S/NF.

Co^{3+} , while the peaks at 781.5 and 797.7 eV are assigned to the Co^{2+} [43]. Generally, the distance between the main peaks and satellite peaks of Co 2p is vital for determining the chemical valence state of Co element. If the chemical shift is ~ 6.0 eV, the cation is Co^{2+} , and the Co^{3+} cation has a distance of 9–10 eV [44,45]. Herein, the spectrum of Co 2p can be well-fitted into four pairs of main peaks with corresponding satellite peaks, which are the characteristics of Co^{2+} and Co^{3+} cations [46]. The Fe 2p spectrum (Fig. 4d) presents two peaks at 724.3 and 710.5 eV, consistent with the $\text{Fe} 2p_{1/2}$ and Fe

$2p_{3/2}$ signals of Fe^{2+} . The two peaks at 713.4 and 716.7 eV demonstrate the presence of Fe^{3+} [19]. The above XPS analysis justify the coexistence of Co and Fe elements with different chemical valence states of (Co^{2+} and Co^{3+}) and (Fe^{2+} and Fe^{3+}) in the product.

The electrochemical performances of as-prepared binder-free electrodes was first investigated in a three-electrode system. Fig. 5a displays the CV curves of two electrodes over a potential window of 0–0.6 V at 10 mV s^{-1} . The existence of redox peaks in both curves demonstrate the presence of faradaic reactions and pseudocapacitive properties of two electrodes. Furthermore, the integral area of the CV curves from Fe-Co-S/NF electrode is much larger than that of CoS/NF electrode, indicating a better electrochemical performance of Fe-Co-S/NF.

To further investigate the superior supercapacitive properties of Fe-Co-S/NF electrode, a series of tests were implemented. Fig. 5b presents the CV curves of Fe-Co-S/NF electrode at $1\text{--}20 \text{ mV s}^{-1}$. Due to the polarization effect, the anodic and cathodic peak positions shift slightly towards the positive potential and negative potential with increasing the scan rate [47]. The same phenomenon also occurs in the CV curves of CoS/NF electrode, as shown in Fig. S6a. According to the previously reported redox reactions of monometal sulfides [12] and MCo_2S_4 [48], the redox peaks caused by the reversible faradaic redox reactions between Fe-Co-S/NF electrode and KOH electrolyte include M-S/M-S-OH and M-S-OH/M-S-O (here M represents Co or Fe), and the possible electrochemical reactions are proposed as follows [19]:

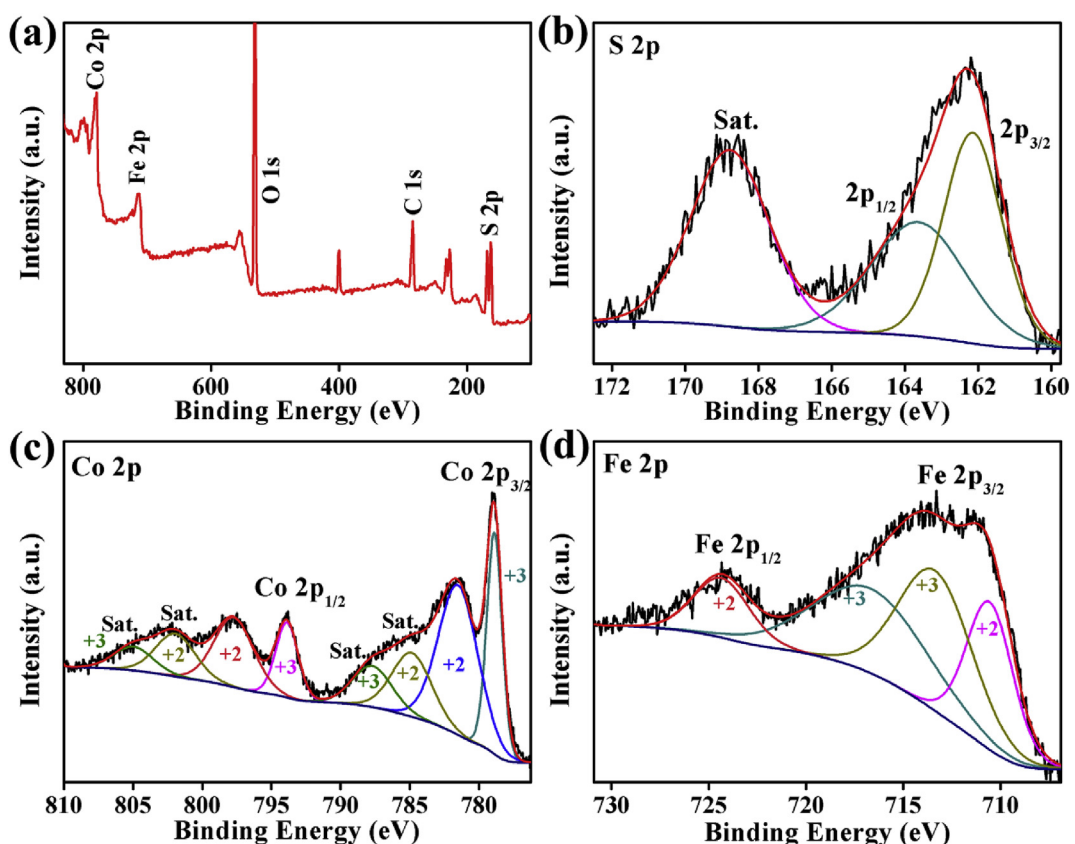


Fig. 4. XPS spectra of (a) the survey spectrum, (b) S 2p, (c) Co 2p, and (d) Fe 2p XPS of Fe-Co-S/NF.

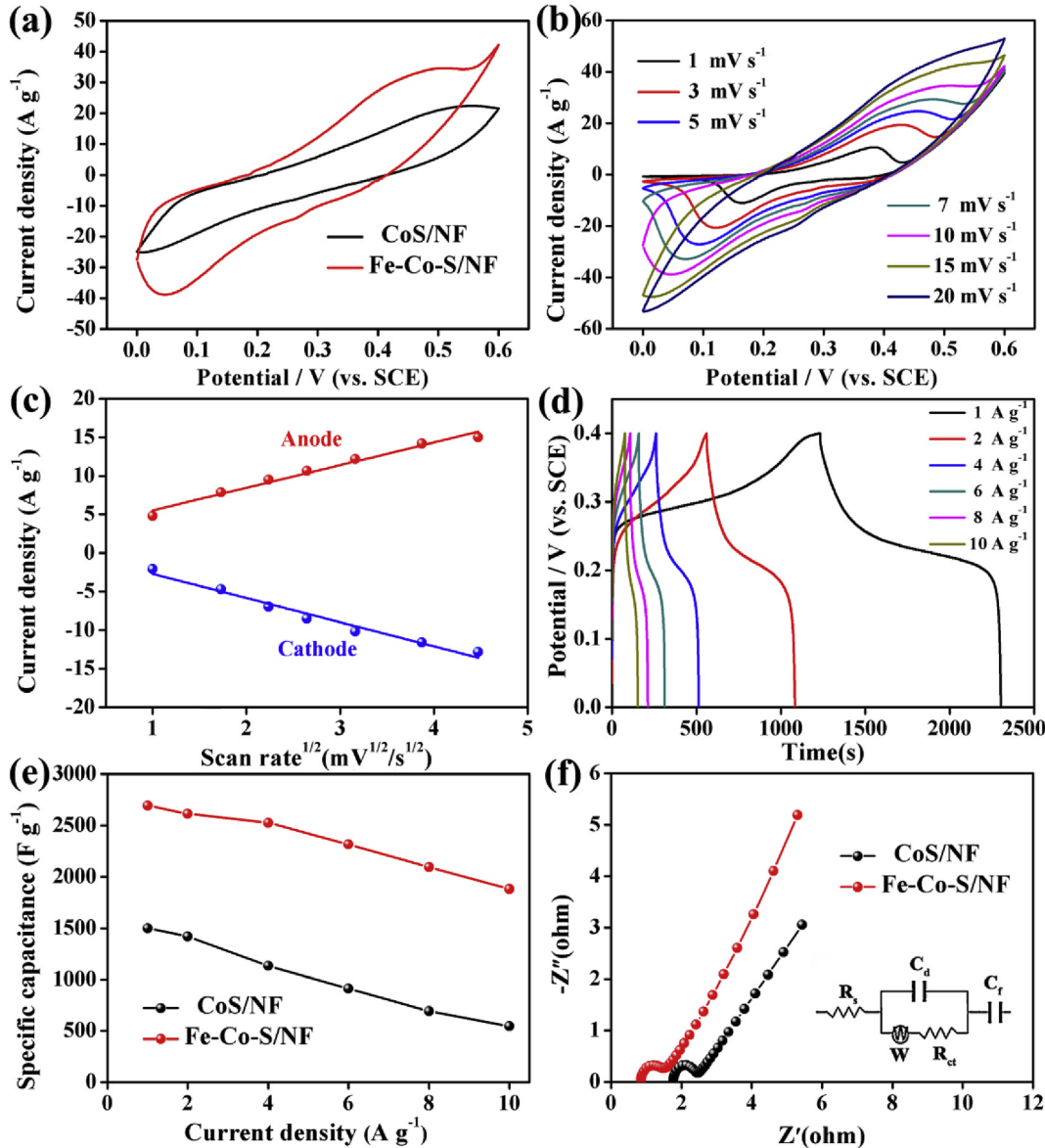
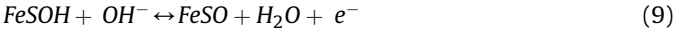
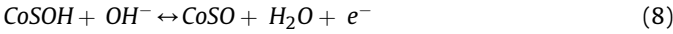


Fig. 5. (a) Comparison of the CV curves of CoS/NF and Fe-Co-S/NF electrodes measured at a scan rate of 10 mV s⁻¹; (b) CV curves of Fe-Co-S/NF electrode at different scan rates; (c) Linear relationship between the anodic/cathodic peak current and the square root of scan rate; (d) GCD curves of Fe-Co-S/NF at various current densities; (e) Specific capacitance of CoS/NF and Fe-Co-S/NF electrodes at different current densities; (f) EIS spectra of CoS/NF and Fe-Co-S/NF electrodes.



Furthermore, the CV curves are also applied to study the electrochemical reaction kinetics of the electrode [49]. The response currents (i) and scan rates (v) conform to Equation (10):

$$i = av^b \quad (10)$$

where a is an adjustable parameter [50]. If $b = 0.5$, the electrochemical process of electrode is a diffusion-controlled redox reaction, whereas $b = 1$ suggests the surface-controlled nature of the redox process [51]. Fig. 5c shows a linear relation between i and $v^{1/2}$, indicating that the value of b is 0.5. Hence, the electrochemical

process of Fe-Co-S/NF electrode is a diffusion controlled redox reaction in the alkaline electrolyte.

The specific capacitance of electrode was investigated by using quasi-symmetric GCD tests at 1–10 A g⁻¹, as shown in Fig. 5d and Fig. S6b. The Fe-Co-S/NF electrode possesses excellent specific capacitances of 2695, 2614, 2526, 2316, 2096, and 1880 F g⁻¹ at 1–10 A g⁻¹, outperforming that of CoS/NF electrode, i.e., 1500, 1420, 1134, 912, 692, and 545 F g⁻¹ (Fig. 5e). Furthermore, a comparison of Fe-Co-S/NF with previously reported transition metal sulfides is shown in Table 1. The results demonstrate that the Fe-Co-S/NF electrode is comparable or superior to others, indicating its excellent electrochemical performance. Besides, the smaller internal resistance (IR) drop of Fe-Co-S/NF electrode implies a higher conductivity of Fe-Co-S/NF electrode, resulting from the higher conductivity of FeCo₂S₄ nanosheets shell (Fig. S7). Generally, the high electronic conductivity could contribute to good rate performance [27]. Thus, it can be clearly observed that the Fe-Co-S/NF electrode

Table 1

Comparison of electrochemical performance of Fe-Co-S/NF electrode with that of previously reported electrodes.

Material	Capacitance	Current density	Electrolyte	Ref.
NiCo ₂ S ₄ /NF	2036 F g ⁻¹	1 A g ⁻¹	1 M KOH	[16]
MOF-CoNi ₂ S ₄	1890 F g ⁻¹	4 A g ⁻¹	2 M KOH	[28]
MOF-Co ₉ S ₈ /NF	1098 F g ⁻¹	0.5 A g ⁻¹	1 M KOH	[35]
FeCo ₂ S ₄ /CNF	2476 F g ⁻¹	1 A g ⁻¹	3 M KOH	[39]
MOF-Ni-Co-S/NF	1407 F g ⁻¹	0.5 A g ⁻¹	1 M KOH	[54]
CoNi ₂ S ₄ -rGO	1680 F g ⁻¹	1 A g ⁻¹	2 M KOH	[55]
Zn _{0.76} Co _{0.24} S/NGN/CNTs	2484 F g ⁻¹	2 A g ⁻¹	6 M KOH	[56]
FeCo ₂ S ₄ /CMF	2430 F g ⁻¹	1 A g ⁻¹	3 M KOH	[57]
NiCo ₂ S ₄ /rGO	1498 F g ⁻¹	1 A g ⁻¹	1 M KOH	[58]
Fe-Co-S/NF	2695 F g⁻¹	1 A g⁻¹	1 M KOH	This work

exhibits a favorable rate capability with 69.8% capacitance retention when the current density is increased 10 times, much higher than that of CoS/NF electrode, *i.e.*, 36.3%. The higher conductivity of Fe-Co-S/NF electrode is further supported by EIS measurement. As shown in the Nyquist plots (Fig. 5f), a semicircle is observed at high frequency and can be an indicator of Faradaic interfacial charge transfer resistance (R_{ct}) generated from the ion transport between the electrolyte and electrode [52]. Typically, the intersection of curve with the horizontal axis represents the bulk resistance (R_s), including the electrode intrinsic resistance and the electrolyte/electrode interfacial resistance [53]. Obviously, the Fe-Co-S/NF electrode exhibits much faster charge transfer and better conductivity ($R_{ct} = 0.56 \Omega \text{ cm}^{-2}$, and $R_s = 0.85 \Omega \text{ cm}^{-2}$) than the CoS/NF electrode ($R_{ct} = 0.69 \Omega \text{ cm}^{-2}$, and $R_s = 1.84 \Omega \text{ cm}^{-2}$). The low charge transfer resistance and bulk resistance is due to the good intrinsic electronic properties of FeCo₂S₄ and the intimate contact between FeCo₂S₄ and Co₃S₄.

The cycling life was further evaluated using GCD technique at 10 A g^{-1} (Fig. S8). The Fe-Co-S/NF electrode can retain 84% of the initial specific capacitance after 1000 cycles, much better than that of CoS/NF electrode, *i.e.*, 70%, indicative of an enhanced cycle stability of Fe-Co-S/NF electrode. The nanoarrays structure is still maintained after cycling test, as shown in Fig. S9. Moreover, the XPS analyses (Fig. S10) of the Fe-Co-S/NF electrode after cycling test demonstrate that there is no noticeable change in the elemental composition and chemical properties of the material.

Comparing the electrochemical reaction mechanism of CoS/NF and Fe-Co-S/NF in Fig. 6, the outstanding electrochemical performances of Fe-Co-S/NF electrode could be mainly attributed to the following reasons: (1) The core-shell hollow nanostructures can significantly improve the performance of Fe-Co-S/NF electrodes due to numerous accessible active sites and the synergistic effects between hollow Co₃S₄ core and FeCo₂S₄ nanosheets shell. (2) Compared with the bare surface of hollow Co₃S₄ nanoarrays in the CoS/NF, the FeCo₂S₄ nanosheets attached on the surface can greatly enlarge the electrode/electrolyte contacting area of the Fe-Co-S/NF electrode, which provides abundant electrochemical active sites and accommodates more double-layer charges. (3) FeCo₂S₄ exhibits a higher electrochemical activity, which leads to a higher capacitance of Fe-Co-S/NF electrode. (4) Benefiting from the high electronic conductivity of FeCo₂S₄, the Fe-Co-S/NF electrode exhibits a much higher electronic conductivity, resulting in a greatly enhanced rate performance. (5) The direct growth of iron-cobalt sulfides nanoarrays on nickel foam avoids the “dead mass” typically encountered in the conventional slurry coating method [59]. Additionally, the strong adhesion between electroactive materials and nickel foam ensures a remarkable cycling stability of the electrode. Overall, Fe-Co-S/NF owns many outstanding advantages to improve the supercapacitive properties.

To demonstrate the practical application of Fe-Co-S/NF electrode, an asymmetric supercapacitor (ASC) was assembled and

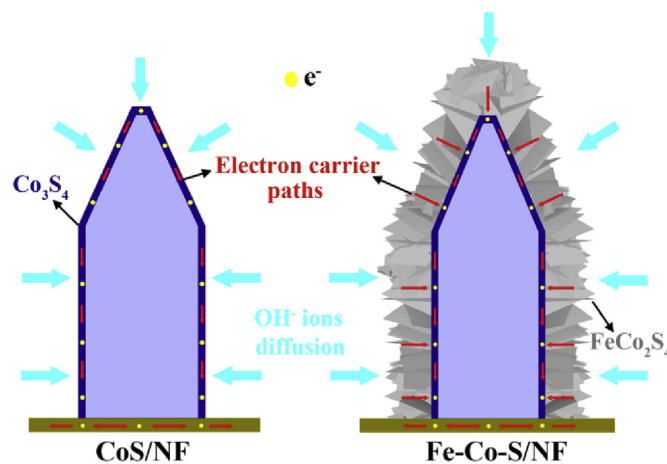


Fig. 6. Electrochemical mechanism of (a) CoS/NF and (b) Fe-Co-S/NF.

tested for its electrochemical performance as presented in Fig. 7a. The SEM image of as-prepared rGO and its electrochemical properties are shown in Fig. S11. The as-prepared rGO is silky (Fig. S11a), and the nearly rectangular shaped CV curves (Fig. S11b) and symmetrical GCD curves (Fig. S11c) suggest that rGO is a typical electric double layer capacitive material. Fig. S11d displays that the rGO electrode exhibits an outstanding specific capacitance of 162 F g^{-1} at 1 A g^{-1} with remaining 81.5% at 10 A g^{-1} , making it a promising candidate for the anode of supercapacitor. The CV curves of Fe-Co-S/NF and rGO electrodes at their corresponding potential range at 10 mV s^{-1} are presented in Fig. S12. Owing to different potential windows of rGO (-1.0 to 0 V) and Fe-Co-S/NF (0 – 0.6 V), the voltage range of ASC device is extended to 1.6 V . According to Equation (2), the mass of rGO and Fe-Co-S/NF is about 16.0 and 2.4 mg , respectively. As presented in Fig. 7b, the non-standard rectangular CV curves of the device at different scan rates indicate the combined contributions of the pseudocapacitance from Fe-Co-S/NF electrode and double-layer capacitance from rGO electrode. Fig. 7c displays the GCD curves of the device at current densities ranging from 1 to 10 A g^{-1} , and the corresponding capacitances based on these GCD curves calculated through equation (3) are presented in Fig. 7d. The ASC device delivers high specific capacitances of 131 and 81 F g^{-1} at the current densities of 1 and 10 A g^{-1} , suggesting a good rate capability of device.

The power and energy densities calculated through equations (4) and (5) are depicted in the Ragone plot in Fig. 7e. The ASC device achieves an excellent energy density of 43.6 W h kg^{-1} at a power density of 770 W kg^{-1} , outperforming many other previously reported devices based on the metal sulfides, such as NiCo₂S₄/NF//AC (35.6 W h kg^{-1} at 819 W kg^{-1}) [16], NiCo₂S₄/CT//AC (40.1 W h kg^{-1} at 798 W kg^{-1}) [60], NiCo₂S₄/NS//AC (25.5 W h kg^{-1} at 334 W kg^{-1})

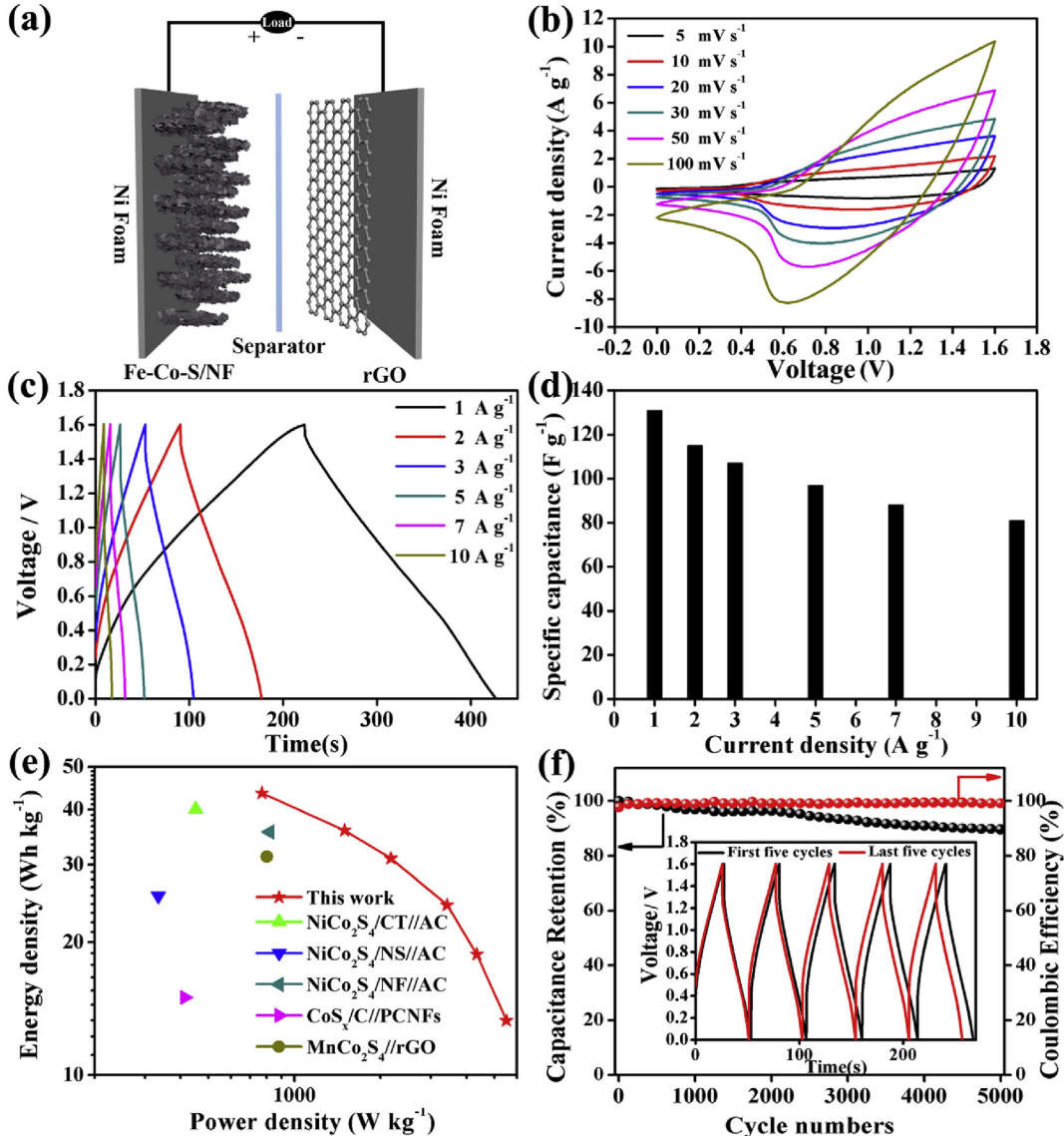


Fig. 7. (a) Fabrication of the Fe-Co-S/NF//rGO ASC device; (b) CV curves of ASC at various scan rates from 0 to 1.6 V; (c) GCD curves of ASC at different current densities; (d) Specific capacitance of ASC at different current densities; (e) Ragone plot of ASC with a comparison to similar ASCs reported previously; (f) Cycling stability and coulombic efficiency of the ASC at 5 A g⁻¹ for 5000cycles. The inset shows the first and last 5 cycles of charge/discharge curves of the ASC.

[61], CoS_x/C//PCNFs (15.0 Wh kg⁻¹ at 413 W kg⁻¹) [62], and MnCo₂S₄//rGO (31.3 Wh kg⁻¹ at 800 W kg⁻¹) [63]. Even at an ultrahigh power density of 5510 W kg⁻¹, an energy density of 13.3 Wh kg⁻¹ is still remained.

Moreover, as shown in Fig. 7f, the cycling stability was tested by GCD technique at 5 A g⁻¹. Remarkably, the specific capacitance can reserve 89.6% of its initial capacitance after cycling for 5000 cycles and nearly 100% Coulombic efficiency throughout the cycling stability test, which is comparable or higher than that of the previously reported ASC devices (See Table S1). The initial and the last 5 cycles of GCD curves (inset in Fig. 7f) reveal a very regular cycling charging-discharging behavior.

4. Conclusions

In summary, hierarchical core-shell hollow iron-cobalt sulfide nanoarrays supported on conductive nickel foam as binder-free electrode for high-performance supercapacitors have been

successfully fabricated through a novel MOF-engaging templated method. Owing to the merits of complex compositional and unique structure, the Fe-Co-S/NF electrode exhibits an ultrahigh specific capacitance of 2695 F g⁻¹ and a favorable cycling stability. The ASC devices assembled with Fe-Co-S/NF (cathode) and rGO (anode) exhibit an excellent energy density of 43.6 Wh kg⁻¹, and an outstanding cycling stability with 89.6% capacitance retention over 5000 cycles. Therefore, this work proposes a novel MOF-engaging templated method for manufacturing hierarchical core-shell hollow hybrid materials as high-performance electrodes of energy storage and conversion devices.

Acknowledgements

The authors acknowledge the financial support from the National Natural Science Foundation of China (No. 51572157 and No. 51502159), the Fundamental Research Fund of Shandong University (2015JC016, 2015JC036, and 2018JC046), the Natural Science

Foundation of Shandong Province (Grant ZR2016BM16), and the Qilu Young Scholar Scheme of Shandong University (No. 31370088963043).

Appendix A. Supplementary data

Supplementary data to this article can be found online at <https://doi.org/10.1016/j.electacta.2019.134826>.

References

- [1] K. Le, Z. Wang, F. Wang, Q. Wang, et al., Sandwich-like NiCo layered double hydroxides/reduced graphene oxide nanocomposite cathode for high energy density asymmetric supercapacitors, *Dalton Trans.* 48 (2019) 5193–5202.
- [2] G. Wang, L. Zhang, J. Zhang, A review of electrode materials for electrochemical supercapacitors, *Chem. Soc. Rev.* 41 (2012) 797–828.
- [3] Y. Ma, C. Hou, H. Zhang, Q. Zhang, H. Liu, S. Wu, Z. Guo, Three-dimensional core-shell Fe_3O_4 /polyaniline coaxial heterogeneous nanonets: preparation and high performance supercapacitor electrodes, *Electrochim. Acta* 315 (2019) 114–123.
- [4] H.S. Chavan, B. Hou, A.T.A. Ahmed, Y. Jo, S. Cho, J. Kim, S.M. Pawar, S. Cha, A.I. Inamdar, H. Im, H. Kim, Nanoflake NiMoO_4 based smart supercapacitor for intelligent power balance monitoring, *Sol. Energy Mater. Sol. Cells* 185 (2018) 166–173.
- [5] A.I. Inamdar, J. Kim, Y. Jo, H. Woo, S. Cho, S.M. Pawar, S. Lee, J.L. Gunjakar, Y. Cho, B. Hou, S. Cha, J. Kwak, Y. Park, H. Kim, H. Im, Highly efficient electro-optically tunable smart-supercapacitors using an oxygen-excess nanograin tungsten oxide thin film, *Sol. Energy Mater. Sol. Cells* 166 (2017) 78–85.
- [6] L. Shen, L. Du, S. Tan, Z. Zang, C. Zhao, W. Mai, Flexible electrochromic supercapacitor hybrid electrodes based on tungsten oxide films and silver nanowires, *Chem. Commun.* 52 (2016) 6296–6299.
- [7] Y. Chen, Z. Liu, L. Sun, Z. Lu, K. Zhuo, Nitrogen and sulfur co-doped porous graphene aerogel as an efficient electrode material for high performance supercapacitor in ionic liquid electrolyte, *J. Power Sources* 390 (2018) 215–223.
- [8] Y. Zhang, Y. An, L. Wu, et al., Metal-free energy storage systems: combining batteries with capacitors based on methylene blue functionalized graphene cathode, *J. Mater. Chem. A* 7 (2019) 19668–19675, <https://doi.org/10.1039/C9TA06734E>.
- [9] S. Yue, H. Tong, L. Lu, W. Tang, W. Bai, F. Jin, Q. Han, J. He, J. Liu, X. Zhang, Hierarchical NiCo_2O_4 nanosheets/nitrogen doped graphene/carbon nanotube film with ultrahigh capacitance and long cycle stability as a flexible binder-free electrode for supercapacitors, *J. Mater. Chem. A* 5 (2017) 689–698.
- [10] B. Kirubasankar, V. Murugadoss, J. Lin, et al., In-situ grown nickel selenide onto graphene nanohybrid electrodes for high energy density asymmetric supercapacitors, *Nanoscale* 10 (2018) 20414–20425.
- [11] W. Du, X. Wang, J. Zhan, X. Sun, et al., Biological cell template synthesis of nitrogen-doped porous hollow carbon spheres/ MnO_2 composites for high-performance asymmetric supercapacitors, *Electrochim. Acta* 296 (2019) 907–915.
- [12] J. Yang, M. Ma, C. Sun, Y. Zhang, W. Huang, X. Dong, Hybrid $\text{NiCo}_2\text{S}_4@\text{MnO}_2$ heterostructures for high-performance supercapacitor electrodes, *J. Mater. Chem. A* 3 (2015) 1258–1264.
- [13] G. Liu, B. Wang, L. Wang, T. Liu, T. Gao, D. Wang, Facile controlled synthesis of a hierarchical porous nanocoral-like Co_3S_4 electrode for high-performance supercapacitors, *RSC Adv.* 6 (2016) 54076–54086.
- [14] H. Wang, M. Liang, D. Duan, W. Shi, Y. Song, Z. Sun, Rose-like Ni_3S_4 as battery-type electrode for hybrid supercapacitor with excellent charge storage performance, *Chem. Eng. J.* 350 (2018) 523–533.
- [15] Z. Gao, C. Chen, J. Chang, L. Chen, P. Wang, D. Wu, F. Xu, K. Jiang, Porous $\text{Co}_3\text{S}_4@\text{Ni}_3\text{S}_4$ heterostructure arrays electrode with vertical electrons and ions channels for efficient hybrid supercapacitor, *Chem. Eng. J.* 343 (2018) 572–582.
- [16] Y. Wen, S. Peng, Z. Wang, J. Hao, T. Qin, S. Lu, J. Zhang, D. He, X. Fan, G. Cao, Facile synthesis of ultrathin NiCo_2S_4 nano-petals inspired by blooming buds for high-performance supercapacitors, *J. Mater. Chem. A* 5 (2017) 7144–7152.
- [17] A. Pramanik, S. Maiti, T. Dhawa, M. Sreemany, S. Mahanty, High faradaic charge storage in ZnCo_2S_4 film on Ni-foam with a hetero-dimensional microstructure for hybrid supercapacitor, *Mater. Today Energy* 9 (2018) 416–427.
- [18] J. Lin, Y. Wang, X. Zheng, H. Liang, H. Jia, J. Qi, J. Cao, J. Tu, W. Fei, J. Feng, P-Doped NiCo_2S_4 nanotubes as battery-type electrodes for high-performance asymmetric supercapacitors, *Dalton Trans.* 47 (2018) 8771–8778.
- [19] S. Tang, B. Zhu, X. Shi, J. Wu, X. Meng, General controlled sulfidation toward achieving novel nanosheet-built porous square- FeCo_2S_4 -tube Arrays for high-performance asymmetric all-solid-state pseudocapacitors, *Adv. Energy Mater.* 7 (2017), 1601985.
- [20] J. Jun, J.S. Lee, D.H. Shin, S.G. Kim, J. Jang, Multidimensional MnO_2 nanohair-decorated hybrid multichannel carbon nanofiber as an electrode material for high-performance supercapacitors, *Nanoscale* 7 (2015) 16026–16033.
- [21] M. Liang, M. Zhao, H. Wang, J. Shen, X. Song, Enhanced cycling stability of hierarchical $\text{NiCo}_2\text{S}_4@\text{Ni}(\text{OH})_2@\text{PPy}$ core–shell nanotube arrays for aqueous asymmetric supercapacitors, *J. Mater. Chem. A* 6 (2018) 2482–2493.
- [22] N. Wu, D. Xu, Z. Wang, et al., Achieving superior electromagnetic wave absorbers through the novel metal-organic frameworks derived magnetic porous carbon nanorods, *Carbon* 145 (2019) 433–444.
- [23] L. Wang, Y. Han, X. Feng, J. Zhou, P. Qi, B. Wang, Metal–organic frameworks for energy storage: batteries and supercapacitors, *Coord. Chem. Rev.* 307 (2016) 361–381.
- [24] H. Furukawa, K.E. Cordova, M. O’Keeffe, O.M. Yaghi, The chemistry and applications of metal-organic frameworks, *Science* 341 (2013) 1230444.
- [25] S. Dang, Q.-L. Zhu, Q. Xu, Nanomaterials derived from metal–organic frameworks, *Nat. Rev. Mater.* 3 (2017) 17075.
- [26] Q. Yang, Y. Liu, L. Xiao, M. Yan, H. Bai, F. Zhu, Y. Lei, W. Shi, Self-templated transformation of MOFs into layered double hydroxide nanoarrays with selectively formed Co_9S_8 for high-performance asymmetric supercapacitors, *Chem. Eng. J.* 354 (2018) 716–726.
- [27] C. Qu, L. Zhang, W. Meng, Z. Liang, B. Zhu, D. Tang, S. Dai, B. Zhao, H. Tabassum, S. Gao, H. Zhang, W. Guo, R. Zhao, X. Huang, M. Liu, R. Zou, MOF-derived alpha-NiS nanorods on graphene as an electrode for high-energy-density supercapacitors, *J. Mater. Chem. B* 6 (2018) 4003–4012.
- [28] Q. Wang, F. Gao, B. Xu, F. Cai, F. Zhan, F. Gao, Q. Wang, ZIF-67 derived amorphous CoNi_2S_4 nanocages with nanosheet arrays on the shell for a high-performance asymmetric supercapacitor, *Chem. Eng. J.* 327 (2017) 387–396.
- [29] K. Tao, X. Han, Q. Cheng, Y. Yang, Z. Yang, Q. Ma, L. Han, A zinc cobalt sulfide nanosheet array derived from a 2D bimetallic metal-organic frameworks for high-performance supercapacitors, *Chem. Eur. J.* 24 (2018) 12584–12591.
- [30] D. Guo, X. Song, L. Tan, H. Ma, H. Pang, X. Wang, L. Zhang, Metal-organic framework template-directed fabrication of well-aligned pentagon-like hollow transition-metal sulfides as the anode and cathode for high-performance asymmetric supercapacitors, *ACS Appl. Mater. Interfaces* 10 (2018) 42621–42629.
- [31] G. Zhu, X. Cui, Y. Zhang, et al., Poly (vinyl butyral)/graphene oxide/poly (methylhydrosiloxane) nanocomposite coating for improved aluminum alloy anticorrosion, *Polymer* 172 (2019) 415–422.
- [32] H. Cao, N. Wu, Y. Liu, S. Wang, W. Du, J. Liu, Facile synthesis of rod-like manganese molybdate crystallines with two-dimensional nanoflakes for supercapacitor application, *Electrochim. Acta* 225 (2017) 605–613.
- [33] T. Li, R. Li, H. Luo, Facile in situ growth of Ni/Co-LDH arrays by hydrothermal chemical coprecipitation for all-solid-state asymmetric supercapacitors, *J. Mater. Chem. A* 4 (2016) 18922–18930.
- [34] G. Yilmaz, K.M. Yam, C. Zhang, H.J. Fan, G.W. Ho, In situ transformation of MOFs into layered double hydroxide embedded metal sulfides for improved electrocatalytic and supercapacitive performance, *Adv. Mater.* 29 (2017), 1606814.
- [35] X. Han, K. Tao, D. Wang, L. Han, Design of a porous cobalt sulfide nanosheet array on Ni foam from zeolitic imidazolate frameworks as an advanced electrode for supercapacitors, *Nanoscale* 10 (2018) 2735–2741.
- [36] Y. Xiao, D. Su, X. Wang, S. Wu, L. Zhou, Z. Sun, Z. Wang, S. Fang, F. Li, Ultrahigh energy density and stable supercapacitor with 2D NiCoAl Layered double hydroxide, *Electrochim. Acta* 253 (2017) 324–332.
- [37] Y. Ma, Y. Wang, D. Xie, Y. Gu, H. Zhang, G. Wang, Y. Zhang, H. Zhao, P.K. Wong, NiFe-layered double hydroxide nanosheet arrays supported on carbon cloth for highly sensitive detection of nitrite, *ACS Appl. Mater. Interfaces* 10 (2018) 6541–6551.
- [38] J. Yu, Q. Wang, D. O’Hare, L. Sun, Preparation of two dimensional layered double hydroxide nanosheets and their applications, *Chem. Soc. Rev.* 46 (2017) 5950–5974.
- [39] Y. Huang, Y. Zhao, J. Bao, J. Lian, M. Cheng, H. Li, Lawn-like FeCo_2S_4 hollow nanoneedle arrays on flexible carbon nanofiber film as binder-free electrodes for high-performance asymmetric pseudocapacitors, *J. Alloy. Comp.* 772 (2019) 337–347.
- [40] S. Li, W. Huang, Y. Yang, J. Ulstrup, L. Ci, J. Zhang, J. Lou, P. Si, Hierarchical layer-by-layer porous $\text{FeCo}_2\text{S}_4@\text{Ni}(\text{OH})_2$ arrays for all-solid-state asymmetric supercapacitors, *J. Mater. Chem. A* 6 (2018) 20480–20490.
- [41] M. Sun, J. Tie, G. Cheng, T. Lin, S. Peng, F. Deng, F. Ye, L. Yu, In situ growth of burl-like nickel cobalt sulfide on carbon fibers as high-performance supercapacitors, *J. Mater. Chem. A* 3 (2015) 1730–1736.
- [42] Y. Wang, Q. Du, H. Zhao, S. Hou, Y. Shen, H. Li, X. Kong, W. Sun, B. Zhang, S. Li, F. Huo, W. Zhang, Metal-organic framework derived leaf-like CoSNC nanocomposites for supercapacitor electrodes, *Nanoscale* 10 (2018) 17958–17964.
- [43] X. Chen, D. Chen, X. Guo, R. Wang, H. Zhang, Facile growth of caterpillar-like NiCo_2S_4 nanocrystal arrays on nickel foam for high-performance supercapacitors, *ACS Appl. Mater. Interfaces* 9 (2017) 18774–18781.
- [44] W. Wei, W. Chen, D.G. Ivey, Rock salt-spinel structural transformation in anodically electrodeposited Mn-Co-O nanocrystals, *Chem. Mater.* 20 (2008) 1941–1947.
- [45] A. Pendashite, J. Palma, M. Anderson, R. Marcilla, NiCoMnO₄ nanoparticles on N-doped graphene: highly efficient bifunctional electrocatalyst for oxygen reduction/evolution reactions, *Appl. Catal. B Environ.* 201 (2017) 241–252.
- [46] S. Wang, Y. Hou, X. Wang, Development of a stable MnCo_2O_4 cocatalyst for photocatalytic CO_2 reduction with visible light, *ACS Appl. Mater. Interfaces* 7 (2015) 4327–4335.
- [47] M. Liang, M. Zhao, H. Wang, J. Shen, X. Song, Enhanced cycling stability of hierarchical $\text{NiCo}_2\text{S}_4@\text{Ni}(\text{OH})_2@\text{PPy}$ core–shell nanotube arrays for aqueous asymmetric supercapacitors, *J. Mater. Chem. A* 6 (2018) 2482–2493.

- [48] X. Liu, Z. Wu, Y. Yin, Hierarchical NiCo₂S₄ @PANI core/shell nanowires grown on carbon fiber with enhanced electrochemical performance for hybrid supercapacitors, *Chem. Eng. J.* 323 (2017) 330–339.
- [49] Y. Liu, X. Teng, Y. Mi, Z. Chen, A new architecture design of Ni–Co LDH-based pseudocapacitors, *J. Mater. Chem. A* 5 (2017) 24407–24415.
- [50] W. Liu, H. Niu, J. Yang, K. Cheng, K. Ye, K. Zhu, G. Wang, D. Cao, J. Yan, Ternary transition metal sulfides embedded in graphene nanosheets as both the anode and cathode for high-performance asymmetric supercapacitors, *Chem. Mater.* 30 (2018) 1055–1068.
- [51] H.-S. Kim, J.B. Cook, H. Lin, J.S. Ko, S.H. Tolbert, V. Ozolins, B. Dunn, Oxygen vacancies enhance pseudocapacitive charge storage properties of MoO_{3-x}, *Nat. Mater.* 16 (2017) 454–460.
- [52] L. Li, K.S. Hui, K.N. Hui, Y.-R. Cho, Ultrathin petal-like NiAl layered double oxide/sulfide composites as an advanced electrode for high-performance asymmetric supercapacitors, *J. Mater. Chem. A* 5 (2017) 19687–19696.
- [53] F. Lai, Y.E. Miao, L. Zuo, H. Lu, Y. Huang, T. Liu, Biomass-derived nitrogen-doped carbon nanofiber network: a facile template for decoration of ultra-thin nickel-cobalt layered double hydroxide nanosheets as high-performance asymmetric supercapacitor electrode, *Small* 12 (2016) 3235–3244.
- [54] K. Tao, X. Han, Q. Ma, L. Han, A metal-organic framework derived hierarchical nickel-cobalt sulfide nanosheet array on Ni foam with enhanced electrochemical performance for supercapacitors, *Dalton Trans.* 47 (2018) 3496–3502.
- [55] Z. Gao, C. Chen, J. Chang, L. Chen, P. Wang, D. Wu, F. Xu, Y. Guo, K. Jiang, Enhanced cycleability of faradic CoNi₂S₄ electrode by reduced graphene oxide coating for efficient asymmetric supercapacitor, *Electrochim. Acta* 281 (2018) 394–404.
- [56] H. Tong, W. Bai, S. Yue, Z. Gao, L. Lu, L. Shen, S. Dong, J. Zhu, J. He, X. Zhang, Zinc cobalt sulfide nanosheets grown on nitrogen-doped graphene/carbon nanotube film as a high-performance electrode for supercapacitors, *J. Mater. Chem. A* 4 (2016) 11256–11263.
- [57] Y. Huang, F. Cui, M. Hua, L. Xu, Y. Zhao, J. Lian, J. Bao, H. Li, Hierarchical FeCo₂S₄ nanotube Arrays deposited on 3D carbon foam as binder-free electrodes for high-performance asymmetric pseudocapacitors, *Chem. Asian J.* 13 (2018) 3212–3221.
- [58] K.P. Annamalai, L. Liu, Y. Tao, Highly exposed nickel cobalt sulfide–rGO nanoporous structures: an advanced energy-storage electrode material, *J. Mater. Chem. A* 5 (2017) 9991–9997.
- [59] C. Guan, X. Liu, W. Ren, X. Li, C. Cheng, J. Wang, Rational design of metal-organic framework derived hollow NiCo₂O₄ arrays for flexible supercapacitor and electrocatalysis, *Adv. Energy Mater.* 7 (2017), 1602391.
- [60] L. Hao, L. Shen, J. Wang, Y. Xu, X. Zhang, Hollow NiCo₂S₄ nanotube arrays grown on carbon textile as a self-supported electrode for asymmetric supercapacitors, *RSC Adv.* 6 (2016) 9950–9957.
- [61] Z. Wu, X. Pu, X. Ji, Y. Zhu, M. Jing, Q. Chen, F. Jiao, High energy density asymmetric supercapacitors from mesoporous NiCo₂S₄ nanosheets, *Electrochim. Acta* 174 (2015) 238–245.
- [62] Y. Liu, J. Zhou, W. Fu, P. Zhang, X. Pan, E. Xie, In situ synthesis of CoS_x@carbon core-shell nanospheres decorated in carbon nanofibers for capacitor electrodes with superior rate and cycling performances, *Carbon* 114 (2017) 187–197.
- [63] S. Liu, S.C. Jun, Hierarchical manganese cobalt sulfide core-shell nanostructures for high-performance asymmetric supercapacitors, *J. Power Sources* 342 (2017) 629–637.